Japanese Journal of
Applied Physics

LETTER • OPEN ACCESS

Geometric influence on field emission characteristics of zirconium carbide nanoneedles

OPEN ACCESS

Japanese Journal of Applied Physics **64**, 040904 (2025) **LETTER**

https://doi.org/**10.35848/1347-4065/adcbf9**

Geometric influence on field emission characteristics of zirconium carbide nanoneedles

Yimeng Wu[1,2], Jie Tang[1,2*], Shuai Tang[3], You-Hu Chen[1], Ta-Wei Chiu[1,2], Ankit Singh[1†], Masaki Takeguchi[1], Ayako Hashimoto[1,2], and Lu-Chang Qin[4*]

[1]*Research Center for Energy and Environmental Materials, National Institute for Materials Science, Tsukuba, Ibaraki 305-0047, Japan*
[2]*Graduate School of Science and Technology, University of Tsukuba, Tsukuba, Ibaraki 305-8577, Japan*
[3]*State Key Laboratory of Optoelectronic Materials and Technologies, Guangdong Province Key Laboratory of Display Material and Technology, School of Electronics and Information Technology, Sun Yat-sen University, Guangzhou, 510275, People's Republic of China*
[4]*Department of Physics and Astronomy, University of North Carolina at Chapel Hill, Chapel Hill, NC 27599-3255, United States of America*

[*]E-mail: tang.jie@nims.go.jp; lcqin@email.unc.edu

[†]Current address: Department of Metallurgical and Materials Engineering at the Central University of Jharkhand, Ranchi, Cheri-Manatu, Ranchi, 835222, India.

Received March 5, 2025; revised March 26, 2025; accepted April 10, 2025; published online April 28, 2025

⟨100⟩ oriented single-crystalline ZrC nanoneedles were successfully fabricated using a dual-beam FIB-SEM system. Atomic characterization of the pristine ZrC crystal confirmed the consistency and uniformity of nanoneedles' crystallographic orientation, ensuring tip stability and precision. Nanoneedles with 10–100 nm tip radii were evaluated as field emitters, yielding field enhancement factors of 1.78×10^7–4.85×10^6 m^{-1} and tip emission areas of 0.93–97.3 nm^2. This work underscores the importance of geometric optimization in improving field emission performance and demonstrates a scalable and efficient method for developing high-performance electron sources for advanced electron-beam applications.

Field emission electron sources are known for their unique working mechanism, where electrons are emitted via quantum tunneling under high electric fields at room temperature.[1,2)] The advantages including high response speed, low energy spread, and low power consumption, have driven research into next-generation emitters to overcome the limitations of current commercial W(310) filaments, such as high vacuum requirements, high work function, and emission instability.[1,3–9)] Achieving the high local electric fields required for field emission involves reducing emitter tip dimensions to enhance electron flux density and lower extraction voltage.[3,10,11)] Additionally, low-work-function materials like LaB_6, and HfC have demonstrated promising field emission performance due to their combined low work function and excellent thermal stability.[12–16)] Tang et al. optimized HfC nanowire emitter tips using FIB milling and extended this approach to fabricating CeB_6 and LaB_6 nanoneedle tips, achieving excellent current stability and a well-converged single emission beam.[17–20)] ZrC, another refractory transition metal carbide with a low work function (3.6 eV), high melting point (3532 °C), and remarkable chemical stability, has been studied since the 1980s for its ability to function under higher pressures than typical field emission cathodes.[21–24)] Recent studies on 1D ZrC nanostructured emitters highlight their high crystallinity, pristine surface, and small tip curvature radii for stable, high-brightness electron beams.[25–27)] Our team fabricated single ZrC nanoneedles as field emission sources using a dual-beam system,[28)] achieving controllable fabrication and robust tip morphology. In this study, we evaluated the consistency of ZrC nanoneedles fabricated via FIB-SEM and reported four sets of field emission sources with tip curvature radii of 10, 25, 50, and 100 nm to investigate the relationship between curvature radius and filed emission characteristics.

A dual-beam focused ion beam (FIB-SEM, Helios 650) fabrication process using ion milling was developed to produce ZrC nanoneedle emitters, achieving both structural robustness and controllable fabrication outcomes.[17,28)] Figure 1(a) illustrates the schematic overview of the controlled fabrication method using FIB-SEM to produce a ZrC field emission nanoneedle as electron source from a single crystal. The ⟨100⟩-oriented ZrC crystal (Crystal Base Co., Ltd.) was rough milled into a lamella and picked up by an Omni probe [Fig. 1(b), scanning ion microscopy (SIM) image]. It was then precisely mounted onto a tungsten (W) needle with a prefabricated platform using Pt deposition. Ga ion milling was applied to modify the lamella, first removing the protective carbon coating and then shaping it into a ZrC nanoneedle emitter. Scanning electron microscopy (SEM, JSM-6500F) and transmission electron microscopy (TEM, JEM-ARM200F, JEM-2100F) were used for microstructural characterization. Figure 1(c) shows the ZrC nanoneedle after FIB milling, with a length over 10 μm and a high aspect ratio. The tip region displays three contrast levels: ZrC (lightest), Pt deposition (darkest), and the W needle (moderate), as indicated on the right. Overall, this fabrication process involves replacing the tip of the W needle with a ZrC single crystal to serve as the field emission emitter. The field emission characteristics were tested in a high vacuum chamber (1×10^{-7} Pa), as shown in Fig. 1(d), designed for field emission and thermal flashing. Before measurement, thermal flashing was performed to remove surface adsorbates and contaminants. A negative field was applied to extract electron emission, and the current was recorded at the picoampere level. A grounded microchannel plate (MCP) placed 5 cm from the emitter recorded the emission current and field emission microscopy (FEM) pattern.

TEM characterization was performed on both the pristine ZrC bulk crystal and the fabricated nanoneedle to confirm

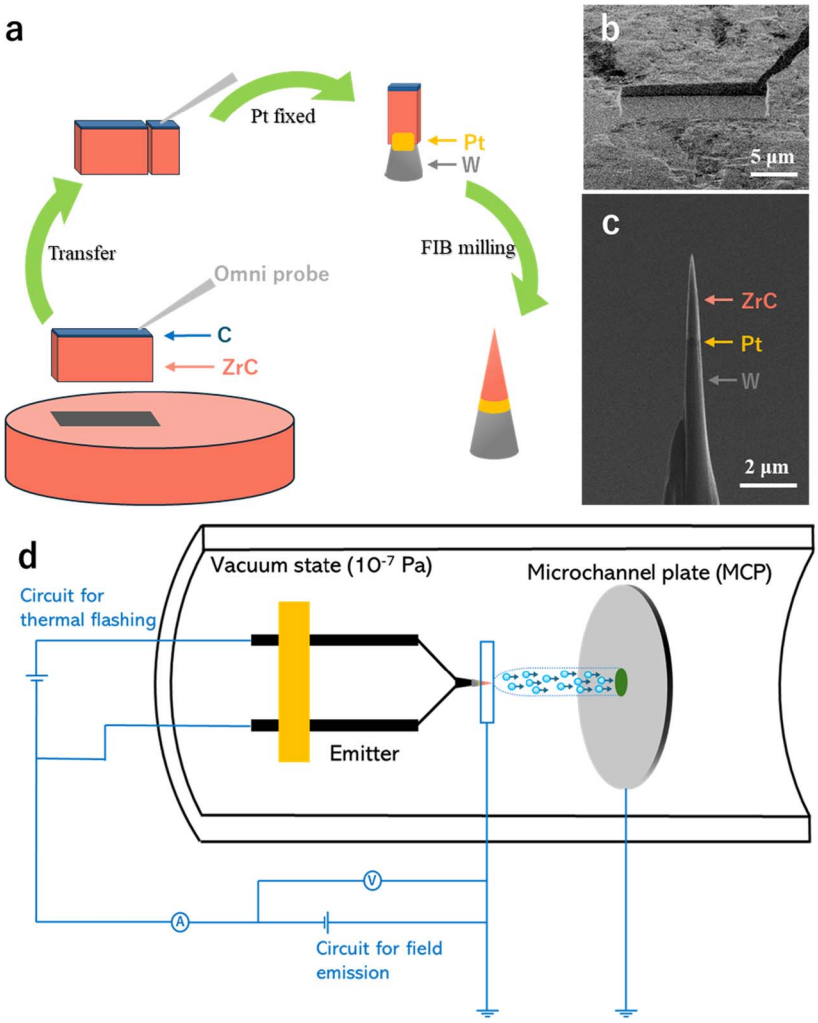

Fig. 1. (a) Schematic illustration of the fabrication process for the ZrC nanoneedle structure. (b) SIM image of the ZrC lamella picked up by an Omni probe from the ZrC bulk material. (c) SEM image of the finished ZrC nanoneedle after fabrication. (d) Experimental setup for field emission measurement.

their single crystallinity. The TEM image of the extracted ZrC lamella [Fig. 2(a)] shows the ZrC crystal with a 600 nm carbon coating applied to prevent Ga ion damage during rough milling. Figure 2(b) presents a high-resolution TEM (HRTEM) image and fast Fourier transform patterns, revealing rotational lattice distortions and a partially crystalline structure located at a depth of 300 nm due to surface oxidation from prolonged air exposure. Fine milling of at least 1 μm was necessary for the ZrC nanoneedle tip to avoid such surface distortions. Further TEM analysis at depths of 1–2 μm [Figs. 2(c) and 2(d)] confirmed the absence of lattice distortions, with lattice spacings of 0.23 and 0.16 nm corresponding to the (200) and (220) planes of the ZrC crystal. Figure 2(e) shows the ZrC nanoneedle after FIB-SEM fabrication, with its tip exhibiting an oxidized amorphous layer from air exposure and Ga ion milling. The inset diffraction pattern aligns with the [001] zone axis of the ZrC crystal, confirming the preservation of single crystallinity at the nanoneedle tip. The HRTEM image of the tip-forming region [Fig. 2(f)] shows a lattice spacing of 0.23 nm, corresponding to the (200) lattice plane. They confirmed the uniformity and single crystallinity of the ZrC bulk and the nanoneedle tip at depths of 1–2 μm. We used energy-dispersive X-ray spectroscopy (EDS) mapping to analyze the chemical composition of the nanoneedle tip. Figure 2(g) illustrates that oxygen is primarily distributed within the amorphous surface layer of the nanoneedle. Figure 2(h) presents the EDS line profile along the axial direction, revealing a gradual decrease in Zr and C concentrations as the diameter decreases, while the O concentration peaks at a depth of 5 nm. This indicates the presence of a 5 nm thick oxidized amorphous layer at the tip, consistent with the observations in Fig. 2(e). This oxidized layer can be minimized and removed during surface pre-treatment in a vacuum chamber. The characterization establishes the stability and consistency of the ZrC nanoneedle tip-forming region, the material properties remain consistent regardless of bulk depth.

The emitter tip curvature radius and the internal crystalline structure influence the field emission properties. During FIB-SEM milling fabrication, the depth of the bulk material utilized varies with the curvature radius, with larger radii corresponding to shallower depths and smaller radii requiring deeper sections of the bulk. Based on the characterizations above, it can be concluded that the curvature radius is the primary factor influencing the field emission characteristics of emitters fabricated using this method.

To examine the impact of tip curvature radius on field emission, we selected ZrC nanoneedles with 10 nm (red), 25 nm (yellow), 50 nm (blue), and 100 nm (green) radii from

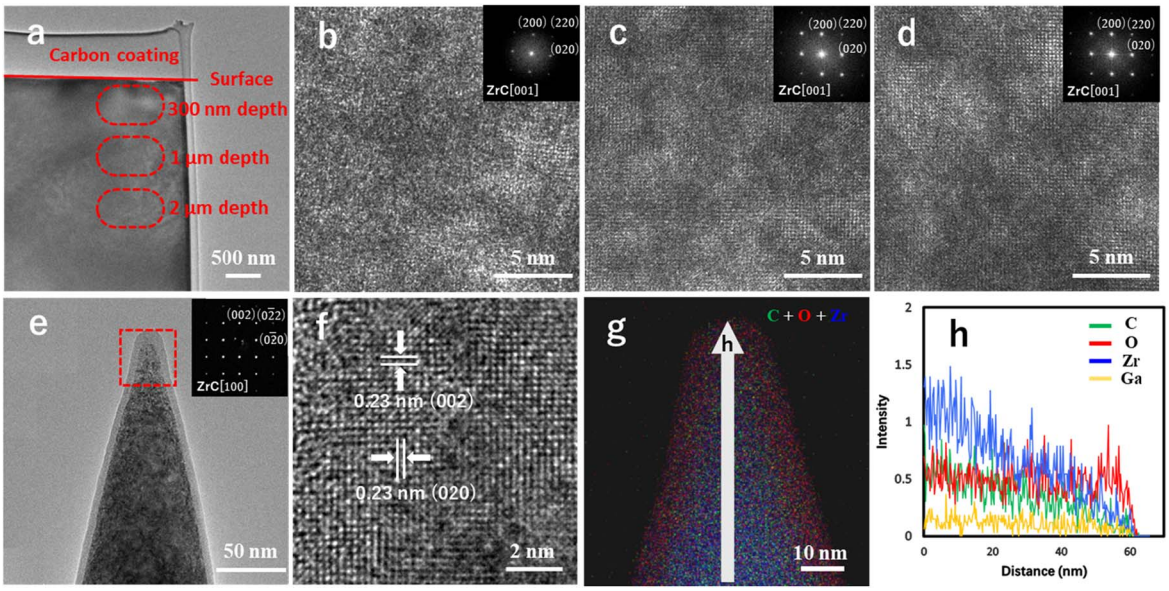

Fig. 2. Structural characterization of ZrC bulk crystal and ZrC nanoneedle. (a) TEM image of the ZrC lamella picked up from the ZrC bulk crystal. (b) HRTEM image of the upper region of the ZrC lamella, corresponding to section below the surface of the ZrC bulk crystal. (c) HRTEM image of the region located 1 μm beneath the surface. (d) HRTEM image of the region located 2 μm beneath the surface. (e) TEM image of the ZrC nanoneedle after completing the FIB milling process. (f) HRTEM image of the tip-forming region of the ZrC nanoneedle. (g) Elemental mapping image corresponding to the overlapping distribution of C (green), O (red), and Zr (blue). (h) Line profiling with the concentrations of C, O, Zr, and Ga shown along the axial direction.

a controlled fabrication process under SEM observation [Fig. 3(a)]. Their field emission properties were then characterized. The tip curvature radii are highlighted with color overlays, consistently used as the legend throughout Fig. 3. All nanoneedles exhibit well-defined geometry, with increasing bluntness as the curvature radius increases.

The ZrC nanoneedles with varying tip curvature radii were tested in a high-vacuum environment (1×10^{-7} Pa), where an extraction voltage was applied to induce field emission. The field emission currents were recorded by internal circuitry. Figure 3(b) displays the emission current (I) versus extraction voltage (V) curves. The data demonstrate that larger tip curvature radii increase the turn-on voltage from 205 to 490 V, while sharper tips yield higher emission currents at the same voltage, emphasizing the role of tip sharpness in field emission. The field emission characteristics

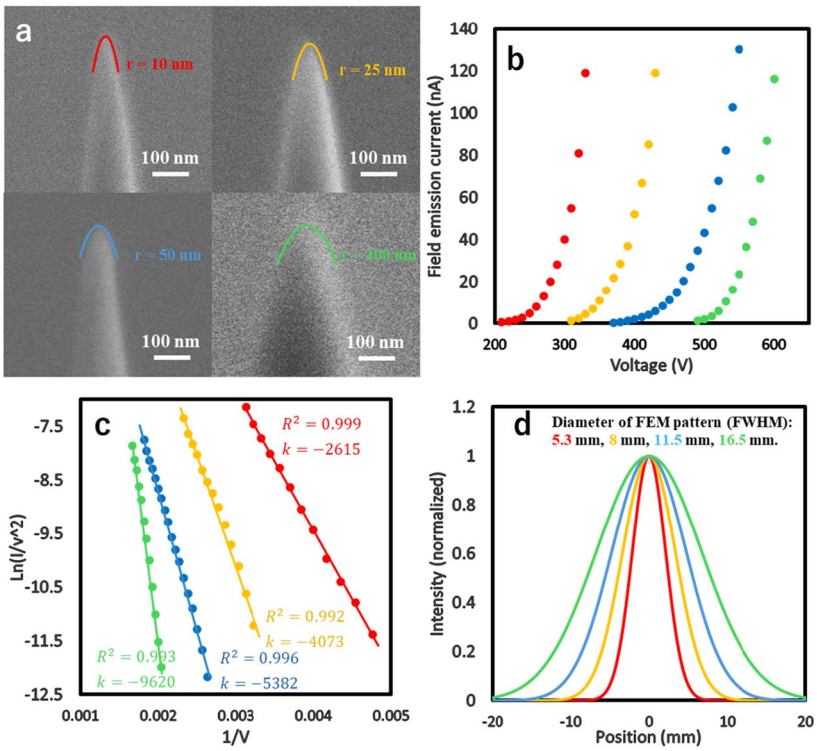

Fig. 3. (a) SEM images of the fabricated ZrC nanoneedles tips with curvature radii of 10 nm (red), 25 nm (yellow), 50 nm (blue), and 100 nm (green). (b) *I*–*V* curves of ZrC nanoneedles with different tip curvature radii. (c) F–N plots corresponding to the *I*–*V* curves in (b). (d) Field emission intensity obtained from FEM pattern normalized by Gaussian distribution.

were evaluated using the Fowler–Nordheim (F–N) equation:[29]

$$I = 1.54 \times 10^{6}\frac{AF^{2}}{\phi}\exp\left(\frac{-6.83 \times 10^{9}\phi^{\frac{3}{2}}}{F}\right), \quad (1)$$

where I is the field emission current, A is the emission area, ϕ is the work function of the emitter surface. By using $F = \beta V$ with β being the field enhancement factor which is determined by the local geometry of the electron emitter, a linearized relationship (F–N plot) is obtained

$$\ln\left(\frac{I}{V^{2}}\right) = -6.83 \times 10^{9}\frac{\phi^{\frac{3}{2}}}{\beta V} + \log\left(1.54 \times 10^{6}\frac{A\beta^{2}}{\phi}\right), \quad (2)$$

and

$$k = 6.83 \times 10^{9}\frac{\phi^{\frac{3}{2}}}{\beta} \quad (3)$$

is the slope of the linear plot. The F–N plots corresponding to the four sets of I–V curves are shown in Fig. 3(c). All fitted trend lines demonstrated a high degree of linearity with R^2-coefficients confirming that the field emission behavior aligns with the cold field emission model. By incorporating the work function of ZrC ($\phi = 3.6$ eV) and the slopes of the four linear functions obtained from the F–N plots, we calculated the corresponding field enhancement factors (β) for the four ZrC nanoneedles. The results indicate that a decrease in β with increasing tip curvature radius: $1.78 \times 10^{7}\,\mathrm{m}^{-1}$, $1.15 \times 10^{7}\,\mathrm{m}^{-1}$, $8.67 \times 10^{6}\,\mathrm{m}^{-1}$, and $4.85 \times 10^{6}\,\mathrm{m}^{-1}$, respectively.

The MCP at the anode recorded FEM patterns of single electron beams emitted from four ZrC nanoneedles under varying voltages. The spot intensity follows a Gaussian distribution, changing with the applied voltage. Figure 3(d) shows the normalized Gaussian distribution curves from FEM patterns, enabling direct comparison of emission beam distributions across different tip diameters. Measurement of the full width at half maximum showed the spot diameters of 5.3 mm, 8.0 mm, 11.5 mm, and 16.5 mm, with corresponding semi-angles of 53 mrad, 80 mrad, 115 mrad, and 165 mrad when the curvature radius increases. FEM parameters indicate electron emission from regions of $\sim$0.93 nm^2, 5.78 nm^2, 23.3 nm^2, and 97.3 nm^2 at 50 nA. These emission areas align with previously calculated field emission characteristics, confirming that smaller curvature radii enhance the local electric fields, reducing the emission area at the ZrC nanoneedle tip. The scattering angle depends on the emission area and tip curvature radius, as variations in the electric field distribution cause smaller curvatures to concentrate the field and reduce emission area, while larger curvatures distribute it more uniformly, leading to a power-law rather than linear relationship.

A balance between the thermal effects and emission noise is achieved in the ZrC nanoneedle emitter through their high thermal stability, mechanical hardness, and overall structural robustness. Generally, reducing the emission area while maintaining a high current leads to emission current instabilities and a shortened emitter lifetime owing to two primary factors: Joule heating more likely occurs at the emitter apex, and the emission current becomes increasingly sensitive to surface roughness. As the emission area decreases, current density rises, causing localized heating that accelerates material evaporation and thermal noise. In addition, the field emission current is highly dependent on the local electric field and the work function of the tip surface. Surface evaporation, atomic adsorption, and contamination at the tip can all degrade the current stability and increase the emission noise. Nevertheless, the ZrC nanoneedle emitter exhibited high emission stability and a prolonged lifetime.[28] Our study reveals that optimizing the tip curvature radius balances thermal effects and emission noise. By fabricating ZrC nanoneedles with a curvature radius as small as 10 nm using the FIB-SEM system, we achieved a clean, low-work-function surface and a structurally stable emitter. After removing the 5 nm thick oxidized layer during the pretreatment, the exposed ZrC single crystal enabled field emission at over 200 V. The intrinsic physical properties of the material including high melting point and hardness, combined with the emitter's structural robustness effectively balanced current instabilities and noise caused by tip morphology. The ZrC nanoneedle emitter exhibited a 100-fold increase in the emission area with a tenfold increase in the tip curvature radius while maintaining a low turn-on voltage and high current density. This balance of emission stability, brightness, and energy efficiency underscores ZrC's potential as a next-generation electron source, particularly for applications such as low-voltage SEM imaging and chemical analysis.

We fabricated ⟨100⟩-oriented single-crystalline ZrC nanoneedles with tip curvature radii of 10, 25, 50, and 100 nm using a dual-beam FIB-SEM system. Structural characterization confirmed the positional stability and geometric precision of the tip. Field emission measurement in a vacuum chamber showed high F–N plot linearity, confirming cold field emission. The field enhancement factors are from 1.78×10^{7} to $4.85 \times 10^{6}\,\mathrm{m}^{-1}$, with emission areas from 0.93 to 97.3 nm^2, indicating that smaller curvature radii enhance local electric fields and emission performance. The ZrC nanoneedle emitter balances structural robustness and surface properties, enabling high-density emission at low turn-on voltage. This makes it promising for low-voltage SEM imaging, chemical analysis, and future electron beam applications.

Acknowledgments This work was funded by National Institute for Materials Science (NIMS), Research Center for Energy and Environmental Materials (GREEN). We also wish to thank the support for the Transmission Electron Microscopy Unit, Surface and Bulk Analysis Unit in NIMS, and "Advanced Research Infrastructure for Materials and Nanotechnology in Japan (ARIM: JPMXP1224NM5231)" of the Ministry of Education, Culture, Sports, Science and Technology (MEXT).

ORCID iDs Yimeng Wu https://orcid.org/0009-0001-9780-8203 Masaki Takeguchi https://orcid.org/0000-0002-0282-6020 Ayako Hashimoto https://orcid.org/0000-0002-1985-7667

1) W. P. Dyke and W. W. Dolan, "Field emission," Adv. Electron. Electron Phys. **8**, 89 (1956).
2) R. Stratton, "Theory of field emission from semiconductors," Phys. Rev. **125**, 67 (1962).

3) G. N. Fursey, "Field emission in vacuum micro-electronics," Appl. Surf. Sci. **215**, 113 (2003).
4) A. V. Crewe, D. N. Eggenberger, J. Wall, and L. M. Welter, "Electron gun using a field emission source," Rev. Sci. Instrum. **39**, 576 (1968).
5) E. D. Donets, "Historical review of electron beam ion sources," Rev. Sci. Instrum. **69**, 614 (1998).
6) K. L. Jensen, D. A. Shiffler, J. J. Petillo, Z. Pan, and J. W. Luginsland, "Emittance, surface structure, and electron emission," Phys. Rev. ST Accel. Beams **17**, 043402 (2014).
7) B. D. Barford and R. R. Rye, "Adsorption of ethylene and hydrogen on tungsten single crystals: flash desorption, adsorption kinetics, and work function changes," J. Chem. Phys. **60**, 1046 (1974).
8) P. W. Tamm and L. D. Schmidt, "Condensation of hydrogen on tungsten," J. Chem. Phys. **55**, 4253 (1971).
9) K. Kasuya, S. Katagiri, and T. Ohshima, "High emission current of 1000 μA at $4 \times 10-10$ Pa from W⟨310⟩ cold field emitter in electron gun," J. Vac. Sci. Technol. B **34**, 042202 (2016).
10) I. Brodie and C. A. Spindt, "Vacuum microelectronics," Adv. Electron. Electron Phys. **83**, 1 (1992).
11) E. W. Muller and K. Bahader, "Field ionization of gases at a metal surface and the resolution of the field ion microscope," Phys. Rev. **102**, 624 (1956).
12) M. Grifoni and P. Hanggi, "Driven quantum tunneling," Phys. Rep. **304**, 229 (1998).
13) D. Gatteschi and R. Sessoli, "Quantum tunneling of magnetization and related phenomena in molecular materials," Angew. Chem. Int. Ed. **42**, 268 (2003).
14) J. Hu, T. W. Odom, and C. M. Lieber, "Chemistry and physics in one dimension: synthesis and properties of nanowires and nanotubes," Acc. Chem. Res. **32**, 435 (1999).
15) H. Zhang, J. Tang, J. Yuan, Y. Yamauchi, T. Suzuki, N. Shinya, K. Nakajima, and L.-C. Qin, "An ultrabright and monochromatic electron point source made of a LaB_6 nanowire," Nat. Nanotechnol. **11**, 273 (2016).
16) K. J. Kagarice, G. G. Magera, S. D. Pollard, and W. A. Mackie, "Cold field emission from HfC (310)," J. Vac. Sci. Technol. B **26**, 868 (2008).
17) S. Tang, J. Tang, T. W. Chiu, W. Hayami, J. Uzuhashi, T. Ohkubo, F. Uesugi, M. Takeguchi, M. Mitome, and L.-C. Qin, "A controllable and efficient method for the fabrication of a single HfC nanowire field-emission point electron source aided by low keV FIB milling," Nanoscale **12**, 16770 (2020).
18) S. Tang, J. Tang, Y. Wu, Y.-H. Chen, J. Uzuhashi, T. Ohkubo, and L.-C. Qin, "Stable field emission current from a CeB_6 nanoneedle point electron source," Nanoscale **13**, 17156 (2021).
19) S. Tang, J. Tang, J. Uzuhashi, T. Ohkubo, W. Hayami, J. Yuan, M. Takeguchi, M. Mitome, and L.-C. Qin, "A stable LaB_6 nanoneedle field-emission point electron source," Nanoscale Adv. **3**, 2787 (2021).
20) S. Tang, J. Tang, E. Okunishi, Y. Ninota, A. Yasuhara, J. Uzuhashi, T. Ohkubo, M. Takeguchi, J. Yuan, and L.-C. Qin, "A stable LaB_6 nanoneedle field-emission electron source for atomic resolution imaging with a transmission electron microscope," Mater. Today **57**, 35 (2022).
21) W. A. Mackie, C. H. Hinrichs, and P. R. Davis, "Preparation and characterization of zirconium carbide field emitters," IEEE Trans. Electron Devices **36**, 2697 (1989).
22) L. N. Grossman, "High-temperature thermophysical properties of zirconium carbide," J. Am. Ceram. Soc. **45**, 236 (1965).
23) H. Holleck, "Material selection for hard coatings," J. Vac. Sci. Technol. A **4**, 2661 (1986).
24) W. A. Mackie, R. L. Hartman, M. A. Anderson, and P. R. Davis, "Transition metal carbides for use as field emission cathodes," J. Vac. Sci. Technol. B **12**, 722 (1994).
25) W. A. Mackie, C. H. Hinrichs, and P. R. Davis, "Preparation and characterization of zirconium carbide field emitters," IEEE T Electron Dev. **36**, 2697 (1989).
26) Y. Wu, J. Tang, S. Tang, Y.-H. Chen, T. Chiu, M. Takeguchi, and L.-C. Qin, "Stable field emission from single-crystalline zirconium carbide nanowires," Nanomaterials **1567**, 14 (2024).
27) T. Chiu, J. Tang, S. Tang, J. Yuan, and L.-C. Qin, "Synthesis and field emission of ZrC nanowire," Mater. Today Commun. **25**, 101240 (2020).
28) Y. Wu, J. Tang, S. Tang, Y.-H. Chen, T. Chiu, M. Takeguchi, A. Hashimoto, and L.-C. Qin, "Stable field emissions from zirconium carbide nanoneedle electron source," Nanomaterials **15**, 93 (2025).
29) R. H. Fowler and L. Nordheim, ", Electron emission in intense electric fields," Proc. R. Soc. London, Ser. A **119**, 173 (1928).